Leakage-audited machine learning versus ETAS for earthquake forecasting in the Sea of Marmara

Basri Kerem Alhan[1] (ORCID 0009-0007-8920-9239) and **Kenessary Khabat**[1] (ORCID 0009-0009-6830-7192)

[1] Sapienza University of Rome, Rome, Italy

Corresponding author: Basri Kerem Alhan (basrikerem@gmail.com), ORCID 0009-0007-8920-9239

This is a non-peer-reviewed preprint submitted to EarthArXiv.

Abstract

The Sea of Marmara's locked central fault lies beneath ~18 million people; the 2025 Mw 6.2 Kumburgaz earthquake renewed forecasting interest. We present a leakage-audited benchmark on a homogenized, strictly causal KOERI catalogue: causality is machine-checkable (a truncated-catalogue self-test), and every comparison is adjudicated by a pre-specified block bootstrap requiring both paired intervals to exclude zero. Four physics forecasters (first-generation, cascade Monte-Carlo, spatially-variable-background, and an independent ETAS inversion) form a stable cluster whose verdicts never move: the first three are mutually inseparable, and first-generation beats the inversion. The ETAS$\times$ML hybrid has no robust standing against them: re-running across a narrow range of one calibration constant swings its verdict versus physics between inseparable and beaten, so the machine-learning stage adds no reliable value over a well-fit ETAS. Two engineered channels (GNSS, dense sub-Mc3 catalogue) gave interval-significant gains a placebo battery voided. The Mw 6.2 cell ranked top-1% all year, but temporal information arrived only with its ML 4.0 foreshock 36 minutes before rupture. CSEP tests show the top-ranked forecasters over-predict counts at the honest calibration; the live 30-day regional M$\geq$6 probability is ~1%.

Keywords: earthquake forecasting; ETAS; machine learning; data leakage; Sea of Marmara;

operational earthquake forecasting; foreshocks; information gain

Non-technical summary

The Sea of Marmara, beneath the roughly 18-million-person Istanbul region, holds a locked fault segment that has not produced a large earthquake since 1766; a moderate (magnitude 6.2) shock struck it in April 2025. We asked a practical question: can routine earthquake data tell us where and when the next large event is likely? A recurring problem in such studies is "data leakage," where information about the answer accidentally reaches the model and inflates apparent skill. We built the forecasting system so this cannot happen and made the safeguard automatically checkable by anyone. Using two decades of Turkish monitoring-agency records, we compared machine-learning models against the standard physics-based aftershock model (ETAS). Machine learning did not outperform the well-tuned physics model, and we report this honestly. The system reliably identifies the dangerous fault cells (the "where") but shows that exact timing (the "when") is fundamentally hard: for the 2025 event a useful warning appeared only with its single small foreshock, less than half an hour before the earthquake. The practical message is a standing map of where large earthquakes are most likely, paired with honest limits on predicting exactly when.

1. Introduction

The Main Marmara Fault, the submarine continuation of the North Anatolian Fault beneath the Sea of Marmara, is the most prominent unbroken segment of a fault system that ruptured progressively westward across the twentieth century in a sequence of large earthquakes that culminated in the 1999 Mw 7.4 İzmit and Mw 7.2 Düzce events to its east. The central portion of the Marmara fault has not produced a major earthquake since 1766, and it lies directly offshore of Istanbul, a metropolitan region of some 18 million people. Long-term renewal calculations place the decade-scale probability of an $M \geq 7$ beneath the sea in the tens of percent (Parsons, 2004), and the fault's persistent locking leaves it a mature seismic gap. Recent work has sharpened this picture: an analysis of nearly two decades of seismicity documents an eastward progression of Mw > 5 events along the fault over the past ~15 years, breaching formerly quiet segments (affecting both creeping and locked sections) in what the authors describe as a steady march toward the city (Martínez-Garzón et al., 2026). The 23 April 2025 Mw 6.2 (Mw 6.3 in some solutions) Kumburgaz earthquake, a strike-slip event at ~6 km depth on the central Marmara segment that triggered several hundred aftershocks within two weeks, is the most recent step in that sequence (Ertuncay et al., 2025). A mature seismic gap, a large exposed population, and an active migrating sequence make short-term forecasting here both consequential and demanding, and make it essential that reported "skill" not itself be an evaluation artifact.

The operational standard for short-term forecasting is ETAS (Ogata, 1988), which models seismicity as a background rate plus self-exciting Omori–Utsu aftershock cascades. ETAS underpins the operational aftershock forecasting now run by national agencies (Hardebeck et al., 2024; Mizrahi et al., 2024). A wave of neural point-process and deep-learning models has been proposed as a more flexible alternative (Dascher-Cousineau et al., 2023), but the most careful head-to-head benchmark to date, EarthquakeNPP, found that neural models do not systematically beat a well-implemented ETAS when the two are compared under consistent, reproducible conditions (Stockman et al., 2026). A parallel review reaches the same conclusion from the methodological side: much of the exceptional skill reported in machine-learning earthquake forecasting is an artifact of data leakage from validation protocols that ignore the causal structure of seismicity, and it sets as a *minimum criterion* for practical utility that a candidate model demonstrably match or beat ETAS under strict, prospective, out-of-sample, likelihood-based evaluation (Jover-Alfaro et al., 2026). We meet that minimum criterion directly: modern ETAS baselines, a pre-specified block-bootstrap rule, and genuine pyCSEP consistency tests.

Chief among those artifacts is data leakage: information flowing from the evaluation target back into the features or the model selection. It is endemic in machine-learning seismicity: oversampling positives before the train/test split, tuning thresholds or kernel half-lives on the test set, ablating features with future information visible, "leakage tests" that never actually permute the target. Because rare large events are the quantity of interest, even a small target leak can manufacture apparent M6 skill that is really base-rate rescaling and that evaporates under forward validation. The stakes are concrete: a 2024 *Scientific Reports* Los Angeles prediction study was retracted in 2026 when its performance was traced to a train/test split that ignored temporal order, exactly the failure mode audited here (Yavas et al., 2024, retracted). We therefore adopt an audit-first design and make the absence of look-ahead *machine-checkable* instead of merely asserted: a truncated-catalogue self-test recomputes every feature from a catalogue truncated to the forecast time and requires the recomputed features to reproduce the stored grid, so any reader can verify feature-level causality directly rather than trusting an assertion of it.

This paper makes seven contributions. First, a leakage-audited benchmark for Marmara, whose causality is enforced by a truncated-catalogue self-test that any reproducer can run, and whose every model comparison is adjudicated by a pre-specified block-bootstrap rule rather than a point estimate. Second, a conditional cascade Monte-Carlo forecaster that replaces first-generation ETAS `expected_counts` with full recursive, spatially anisotropic simulation. Third, a benchmark against modern ETAS baselines (an independent third-party inversion and an EM-declustered spatially-variable-background ETAS), which are mutually inseparable and *stable*, whereas the ETAS$\times$ML hybrid's standing against them is unstable to a single operational calibration constant: the machine-learning stage adds no robust value over a well-fit ETAS. Fourth, a placebo battery for engineered feature channels that exposes apparently significant information gains (from a trajectory-modelled GNSS channel and a dense sub-Mc3 catalogue) as noise; it gives a feature-engineering-robust null and a transferable validation method. Fifth, a renewal-informed synthetic training scheme for a conditional large-event discriminator, because the real catalogue contains too few large events to train on directly. Sixth, an information-arrival analysis that freezes the forecast at successive lead times to quantify when, and through which observable, a target becomes visible above background; applied to the 2025 events, it splits the problem into a mature spatial part and a foreshock-bounded temporal part. Seventh, a running hashed, append-only prospective protocol, so that future forecasts accrue genuine out-of-sample credibility that cannot be gamed by hindsight. Together, these seven are the instrumentation of one experiment: whether, under machine-checkable causality, machine learning adds forecasting value beyond modern ETAS for Marmara and, where it does not, what information the catalogue actually carries. Throughout, we report probability *gain* relative to base rates and retain the negative results.

2. Data and study region

Region and grid. The model box spans 25.6–30.9° E and 39.6–41.9° N, chosen to cover the Main Marmara Fault system and the northern strands of the North Anatolian Fault where the KOERI network is densest, so that completeness is as low and as uniform as the data allow (Martínez-Garzón et al., 2026). Forecasts are made on a 0.1° grid (1,219 model-box cells) in 30-day windows; the 0.1° spacing (~8–11 km at these latitudes) is a compromise between fault-scale spatial resolution and having enough events per cell for stable feature estimation, and the 30-day window matches the horizon at which first-generation aftershock forecasting is reliable. For rare-event training only, we additionally use a wide box (25.0–31.5° E, 39.0–42.5° N, 2,275 cells) that captures more M≥4.5 events (including the 2011 Simav, 2013 Aegean, 2014 Gökçeada, 2022 Düzce, and 2025 Sındırgı events) without changing the evaluation region; models trained on the wide box are always evaluated on the model box alone. The Sındırgı sequence lies south of the model box and is therefore used only as an out-of-box coverage check, a limitation we return to in the results.

Catalogue. We derive a homogenized, deduplicated catalogue from the KOERI regional bulletin, 2003-01-04 to 2026-07-11 (frozen as of this fetch; the recent tail is preliminary), comprising 31,360 events in the model box. Three data-level faults in the source were corrected before any modelling. (1) Timestamps in the bulletin are in Türkiye local time but had been treated as UTC; they were converted to true UTC and verified empirically by matching a well-recorded anchor event's origin time to its independently reported UTC time, fixing the offset for the whole catalogue (the proof is recorded in `data/fetch_manifest.json`). An uncorrected three-hour timestamp error would silently corrupt every time-since-last-event and short-window count feature. (2) A single, untyped magnitude column pooled ML, Md, Mw, and Ms without conversion; magnitudes were typed and homogenized to a proxy-moment magnitude (`mag_w`) using the empirical relations of Kadirioğlu and Kartal (2016), applied (and flagged) slightly below their stated validity ranges for a small tail. Because the ML$\rightarrow$Mw and Md$\rightarrow$Mw offsets differ, this typing is what makes the completeness mixture (below) tractable and keeps the M$\geq$3.5 and M$\geq$4.5 targets on a single, consistent scale. (3) 11,754 rows flagged in the source bulletin as suspected quarry blasts (KOERI event type 'Sm') were screened out; counting anthropogenic blasts as tectonic seismicity would bias both the background rate and the feature counts. The audit that motivated these corrections is documented in the repository (`docs/AUDIT.md`).

Completeness. The max-curvature magnitude of completeness is Mc = 3.65 (mode 3.45 + 0.2; Wiemer & Wyss, 2000). This value is *inflated* by ~15,000 Md events piling near `mag_w` 3.45, because the Md$\rightarrow$Mw offset is steeper than ML$\rightarrow$Mw; the dominant modern ML population itself completes near `mag_w` 2.72. Because our targets are defined on `mag_w`, the M$\geq$3.5 target (y35) remains above ML-population completeness and the M$\geq$4.5 target (y45) is far above Mc. Mc is applied identically to feature counting and to every baseline (fair). The mixed-catalogue character makes the Gutenberg–Richter b-value the dominant source of M6 extrapolation uncertainty, and the estimated b is itself sensitive to catalogue-processing choices such as declustering, which can shift the mainshock size distribution materially (Mizrahi et al., 2021); we therefore carry a b-value ensemble: Aki (1965) maximum-likelihood b $\approx$ 1.02, a b-positive estimate $\approx$ 1.54 (van der Elst, 2021), and a calibration-consistent operational b_op = 1.15 (real-window regression slope $\approx$ 1.01). Model-box counts are 5,024 events $\geq$ 3.5, 192 $\geq$ 4.5, 12 $\geq$ 5.5, and a single M $\geq$ 6 (the 2025 Mw 6.2). The single real M6 is why every M6 number in this study comes from Gutenberg–Richter extrapolation, synthetic validation, and wide-box percentile checks, never from a classifier trained on one positive.

Fault model and stress sources. The active-fault geometry is taken from the GEM Global Active Faults Database (Styron & Pagani, 2020), reduced to 97 segments in the region, each with a strike used both to orient anisotropic aftershock kernels and to define Coulomb receiver planes. Time-causal Coulomb stress changes (ΔCFS) are computed with a pure-numpy Okada (1992) half-space dislocation solution and King, Stein, and Lin (1994) resolution of the stress tensor onto per-segment receivers of the form $\Delta\text{CFS} = \Delta\tau + \mu'\Delta\sigma_n$, with rupture geometries for the principal sources taken from published finite-fault models (Table S1). Only ruptures preceding the forecast time contribute, preserving causality. Source parameters for the largest ruptures cite the primary studies (Table S1 lists the principal stress sources): Barka et al. (2002) for the 1999 İzmit slip model, Karabulut et al. (2021) for the 2019 Silivri/Kumburgaz-basin sequence, and Ertuncay et al. (2025) together with the USGS moment tensor for the 2025 Mw 6.2. Interseismic strain is taken as a static field derived from Nevada Geodetic Laboratory GNSS velocities (Blewitt et al., 2018); we treat it as time-invariant by design and later test (and reject) its marginal predictive value. The historical record of M~7 Marmara earthquakes (1509 Mw~7.2 central Marmara; 1719 and 1999 on İzmit; 1754 and 1766 on the Çınarcık/Princes Islands segments; the second 1766 event on Ganos; 1894 on Princes Islands/Yalova; 1912 on Ganos/Mürefte) follows Ambraseys (2002) and Parsons (2004) and anchors the Brownian- Passage-Time renewal layer.

3. Methods

Features and the leakage self-test. Each (cell, window) carries 19 strictly causal features (Table S2 lists the groups): multi-scale event counts (30/90/365 d, in-cell and in 3- and 5-cell neighbourhoods), times since the last M≥3.5 and M≥4.5 within 25 km, local b-positive, a short-/long-term rate ratio, mean depth, distance to the nearest fault, and the time-causal ΔCFS. All features use only events with time < t0. The central methodological safeguard is a truncated-catalogue leakage self-test: for a sample of 26 (cell, t0) rows, every feature is recomputed from a catalogue truncated to < t0; the integer count features must reproduce the stored grid exactly and the remaining real-valued features to a 10^{-6} tolerance, and no feature may correlate > 0.999 with any target. Because the test recomputes features while reusing the fitted model parameters, it gates event-level look-ahead in the features themselves, not parameter-level leakage from fitting decisions (a distinction we return to in §6). Unlike a target-permutation check, which can miss look-ahead that is not target- correlated, this self-test makes feature-level causality a gate any reader can run directly.

ETAS and a null incompleteness correction. We fit an in-house space–time ETAS by maximum likelihood (Ogata, 1988). The conditional intensity at location $\mathbf{x}$ and time t is $\lambda(\mathbf{x},t) = \mu(\mathbf{x}) + \sum_{i:t_i<t} K\, e^{\alpha(m_i-m_c)}(t-t_i+c)^{-p} f(\mathbf{x}-\mathbf{x}_i;m_i)$, a background rate μ plus self-exciting Omori–Utsu aftershock terms with productivity $K\, e^{\alpha(m_i-m_c)}$, temporal decay governed by (c, p), and a spatial kernel f whose scale grows with parent magnitude. The background is estimated in the spirit of the stochastic-declustering approach of Zhuang et al. (2002), and the branching structure is validated against Veen and Schoenberg (2008)-style recovery tests. The implementation passes 5/5 unit tests: recovery of known parameters from simulated catalogues, causal filtering (events at or after t0 never affect a forecast), Omori decay of the triggered rate, and Gutenberg–Richter consistency of the simulator's magnitude output. The branching ratio (the expected number of direct offspring per event) is capped subcritical at 0.95 under the b-positive law used in fitting (b = 1.54). The operational cascade, however, draws offspring magnitudes at the calibrated b_op = 1.15 (or, across the ensemble, at b = 1.02) with the productivity K and α unchanged, which makes the *effective* branching ratio formally supercritical (1.22 at b_op = 1.15 and 1.41 at b = 1.02), so the simulation is stabilised by a 50,000-event per-realisation cap, not by subcriticality. This supercriticality is conditional on the operational magnitude law and is consistent with the cascade's out-of-sample over-prediction of the M≥3.0 count (§4). We attempted a short-term aftershock-incompleteness (STAI) correction using a time-varying completeness Mc(t) (Helmstetter et al., 2006) and raised the branching cap from 0.95 to 0.999 to test whether the maximum-likelihood estimate would leave the cap. Both attempts returned null results: at base Mc = 3.0 the post-M5.5 incompleteness window is sub-hour, so the STAI correction dropped 0 events (consistent with the ETASI formulation of Hainzl et al. (2024), which un-pins only at a low base Mc); and raising the cap did not un-pin the fit: the estimate went straight to the new cap (the documented degenerate near-critical mode). We therefore retain the 0.95 cap for stable simulation, applied identically to the feature ETAS and the ETAS baseline.

Cascade Monte-Carlo forecaster. For each window [t0, t0+H) we forward-simulate new background events plus residual-Omori offspring of all prior history plus full recursive cascades, vectorized across K sims (K = 500 in backtests, 10,000 live; the first logged prospective entries used K = 8,000). Per-cell rare-magnitude rates are computed analytically from the dense M≥3.5 rate field via Gutenberg–Richter, $\lambda_{\text{cell}}(M \geq X) = \lambda_{\text{cell}}(M \geq 3.5) \cdot 10^{-b(X-3.5)}$, which removes the Monte-Carlo $\lambda 6$ = 0 artifact. Offspring of M≥5.5 parents are placed with an elliptical 3:1 kernel oriented along the parent's first-72 h aftershock principal axis (or the nearest fault strike); smaller events are isotropic. This design follows the simulation-based operational-forecasting literature (Hardebeck et al., 2024; Mizrahi et al., 2024). The forecaster passes a four-part gate: (a) future events change nothing (causal); (b) the reliability slope on synthetic catalogues is 0.949, within [0.8, 1.2]; (c) the day-after-M6 rate is 1.79× the first-generation `expected_counts`, quantifying how first-generation ETAS under-counts active sequences; and (d) anisotropy elongates M≥5.5 offspring along-strike 2.77× (vs 1.06 isotropic).

Hybrid and baselines. The hybrid rate is the log-linear blend $\lambda = \lambda_{\text{sim}}^{1-w} \cdot \lambda_{\text{ML}}^{w}$, where λ_sim is the cascade rate, λ_ML is a Poisson gradient-boosted regression on the 19 features plus ln(λ_sim), and the single scalar weight w ∈ [0, 1] is selected on the **validation** per-event log-likelihood. The blend is conservative: w is bounded and chosen out-of-sample, so when the ML stage adds no validated value the hybrid degenerates to the pure cascade (w → 0) and *structurally cannot lose* to its physical core on the validation objective. Monotonicity constraints tie higher ETAS rate and shorter fault distance to higher predicted probability, preventing the booster from learning non-physical inversions (the separate wide-box M≥4.5 production variant, trained on a different feature set, does not impose them). We compare against four baselines (Poisson climatology, fault-proximity, smoothed seismicity, and the ETAS simulation) and, separately, first-generation ETAS `expected_counts`, so that the cascade's contribution is isolable from the ML stage's. Windows are split by start time into training (≤ 2021-12-31), validation (2022–2023), and test (2024-01-01 onward, with the target window fully inside reviewed data, t0 + 30 d ≤ 2026-03-31); the split is strictly temporal so that no future window informs a past one. The preliminary catalogue tail is used only by the live forecast, never in any metric.

Modern ETAS baselines. So that the comparison is against modern physics rather than a strawman, we add two further ETAS forecasters. The spatially-variable-background ETAS (sv-ETAS) re-estimates the background field by expectation–maximization stochastic declustering (Zhuang et al., 2002): each event is probabilistically assigned to background or triggered, and $\mu(\mathbf{x})$ is a Gaussian-kernel density (Silverman bandwidth, 5 km floor) of the background-weighted epicentres, iterated to convergence. The independent Mizrahi ETAS is fit with the third-party `etas` inversion package in an isolated environment and its first-generation intensity is integrated on our grid, providing a comparator whose implementation shares no code with ours. Two integration choices matter for its absolute calibration: we replace its spatially variable background with a uniform floor, and its b-positive estimate on the mixed Md/ML catalogue (b = 1.76) over-weights small magnitudes; both contribute to its magnitude-test failure in §4 alongside the missing secondary triggering. sv-ETAS turns out to be statistically indistinguishable from our first-generation model at both targets. This reflects a property of the catalogue, not an EM degeneracy: the first-generation background is *already* strongly spatially variable (spatial coefficient of variation 1.27; Figure S1); the EM converged in eight iterations with a stable log-likelihood and a physical background fraction of 0.34, so the two backgrounds coincide because the simpler one was already spatially adaptive.

GNSS deformation channel and the placebo battery. We engineered a geodetic channel from 22 continuous-GPS stations (Nevada Geodetic Laboratory IGS20 solutions): per-component trajectory models (secular rate + annual/semiannual terms + antenna/earthquake steps) fit *only* on epochs earlier than 365 days before each forecast window, a common-mode filter, inverse-distance interpolation, and a Delaunay strain-rate field; every feature passes the truncated-catalogue causality gate bit-for-bit. Because a deformation feature can enter the machine-learning stage through spurious structure rather than physical signal, we adjudicate it with a placebo battery: the channel must beat time-shuffled, circularly-shifted ($\geq$ 2 yr), and coverage-only surrogates of itself, each with full retraining. Independent EPOS/MIDAS secular velocities cross-validate the trajectory fits (after removing the expected ~24 mm/yr IGS20-versus-Eurasia frame offset, station residuals are below 1 mm/yr). The battery is a general safeguard for any engineered channel; as the results show, it is decisive here.

Metrics. The headline metric is information gain (IG) in nats per observed event relative to a baseline: the mean difference in Poisson log-likelihood per event between the model and the baseline, $\mathrm{IG} = (1/N)\sum[\ln L_{\mathrm{model}} - \ln L_{\mathrm{base}}]$, computed through one shared scoring function for the model and every baseline so that no predictor enjoys a private evaluation path (Rhoades et al., 2011). A positive IG means the model assigns more probability, per observed event, to where events actually occurred. We also report precision–recall AUC (the discriminative metric most sensitive to the rare positive class), ROC-AUC, and the Brier score, plus reliability diagrams for calibration; Molchan/area-skill trajectories (Zechar & Jordan, 2008) are computed with every evaluation and archived alongside it. Because IG and PR-AUC emphasise different things (likelihood mass versus rank ordering), we treat a result as robust only when the two agree, and flag cases (such as the sparse model-box y45) where they do not.

Statistical inference and the claim rule. Model comparisons follow a rule fixed before the *final* evaluation reported here. For each ordered pair of forecasts and each target we resample the 26 test windows with a Politis–Romano stationary block bootstrap (Politis & Romano, 1994; mean block length three windows, B = 2000 replicates, seed 42), keeping all 1,219 cells of a window together in every draw. The windows tile at 30-day steps and, though the targets are non-overlapping, they are temporally dependent through shared feature history and aftershock clustering, so an independent row-level bootstrap would badly understate the variance: in the repository's worst-case bootstrap audit (perfect within-window correlation) the block interval is about seven times wider than the row interval. We take the 2.5/97.5 percentiles of the paired difference in information gain and in PR-AUC as the 95% confidence interval and declare that A beats B only if both intervals exclude zero in A's favour; otherwise the pair is *inseparable*. All 168 pairwise verdicts are emitted to a machine-readable claims file, and no ranking is stated in this paper that the file does not license. We designate M≥3.0/30-day as the primary powered target (592 test positives), M≥3.5 as a powered secondary (167 positives), and the model-box M≥4.5 as unpowered (no ranking claims). In the interest of full disclosure, this rule and the M≥3.0 primary-endpoint designation were fixed before the *final* evaluation but not before the test set was ever scored: an earlier exploratory pass computed test-split metrics before the block-bootstrap rule and the endpoint choice were set. We mitigate this in the two ways that matter: every tuned hyperparameter (the hybrid weight w and the smoothing σ) was selected on the validation split alone, and every repeated test-set scoring was a deterministic, identical-configuration reproduction rather than a re-tuning, so the reported comparisons are not the product of test-set optimisation.

CSEP consistency tests. We assess consistency with observed seismicity using the catalog-based CSEP tests of Savran et al. (2020), namely number (N), magnitude (M), spatial (S) and pseudo-likelihood (PL), computed with the community pyCSEP toolkit (Savran et al., 2022). Each forecast supplies 1,000 stochastic catalogues built by Poisson-sampling its per-cell $M \geq 3.0$ rate over the test period and drawing Gutenberg–Richter magnitudes at a fixed b = 1.2 for the cascade and sv-ETAS (distinct from the operational b_op = 1.15 that sets their per-cell rates) and at the Mizrahi inversion's own fitted b = 1.76; the same statistics are implemented independently as a cross-check, and the two agree on the N and M verdicts for every model. Because the Poisson (cell-independent) catalogues under-disperse relative to real clustering, we interpret the N and M tests and report S and PL only with that caveat.

Synthetic large-event layer. Because the model box contains a single M6, we train a conditional "bigger-event-ahead" discriminator on synthetic sequences. From 250 base ETAS simulations, each seeded with Brownian-Passage-Time-timed (Matthews et al., 2002) characteristic mainshocks of M ~ U(6.8, 7.6) on the four segments (each with a full aftershock cascade), we take 31,705 snapshots 1/3/7 days after every simulated $M \geq 4.5$; the label is a subsequent simulated event $\geq$ (largest-so-far $-$ 0.3) within 30 days. Features are seismicity-only (b-positive drop, sequence count, largest magnitude, time since start, distance to nearest segment).

Alert and renewal layers. A Foreshock Traffic-Light System (Gulia & Wiemer, 2019) flags relative b-value drops within a sequence; we treat it as an alert layer, not a rate multiplier, and print the low-coverage pseudo-prospective caveat established for the FTLS (Gulia et al., 2020). A Brownian-Passage-Time renewal layer (Matthews et al., 2002; Parsons, 2004) supplies segment-level 30-year conditional M~7 probabilities; it is a large-event layer only and is never blended into the y35/y45 products.

Information-arrival analysis. To characterise *when* a target event becomes forecastable, we define a general procedure that is independent of any single event. For a target (time T, location), we freeze the system at a schedule of strictly causal lead times (e.g. T−365 d, T−180 d, . . . , T−1 h, and just after any foreshock), recompute all products using only data available at each freeze, and track three quantities as functions of lead time: the target cell's spatial percentile among all cells, the per-cell probability *gain* over a uniform baseline, and the conditional discriminator score. The resulting curves separate persistent spatial hazard (flat percentile) from transient temporal information (a jump in gain when an informative event arrives). We apply the analysis to the 2025 Marmara events; every freeze is checked to use only pre-freeze data.

Prospective protocol. A monthly job issues a 30-day forecast at the catalogue end, appends it to an append-only log, and scores past forecasts once their windows close, giving out-of-sample credibility that a backtest cannot. Each entry carries a sha256 content hash written before the outcome is known, so it cannot be silently revised: the log is a commitment device, not a retrospective fit. The catalogue is advanced each month from the KOERI preliminary monthly feed; because the preliminary tail is untyped, it enters only the features of the live forecast and never the reviewed-data evaluation.

4. Results

We organise the results around the pre-specified decision rule and the power of each target. After the catalogue and its completeness we present the primary powered target (M≥3.0), where the rule can resolve model differences; then the M≥3.5 replication and the unpowered M≥4.5 diagnostic; then CSEP consistency and the engineered non-catalogue channels; and finally calibration, the conditional large-event layer, the information-arrival analysis for the 2025 events, and the live products. Throughout, the relevant comparison is against modern, properly-fit ETAS variants, not naive baselines, every ranking is licensed by the block-bootstrap rule of §3, and the single model-box M6 caps how strong any large-event claim can be.

Catalogue and completeness (Table S3). The processed catalogue and its completeness structure are summarized in Table S3; the key operational fact is the single model-box M6, which forces every large-event number to rest on extrapolation and simulation instead of direct classification.

Primary target: M≥3.0/30-day (Table 1). The M≥3.0 target carries the most test positives (592) and is where the pre-specified rule has the power to separate models. The physics forecasters cluster at the top (sv-ETAS PR-AUC 0.229, cascade 0.228, first-generation 0.223, Mizrahi 0.206), and at the honest operational calibration (b_op = 1.15; §3) the ETAS×ML hybrid sits with them (0.218; Figure 1). Under the rule the hybrid is inseparable from all four physics models: its information gain matches or exceeds theirs (e.g. hybrid vs cascade +0.49 nats [+0.41, +0.61]) while its PR-AUC deficit is not significant, and it clearly beats the non-clustering baselines (vs smoothed +0.09 PR-AUC [+0.07, +0.12]). Within the physics cluster, cascade, sv-ETAS, and first-generation ETAS are mutually inseparable, and first-generation ETAS separably beats the Mizrahi inversion (information gain −0.36 [−0.57, −0.14], ΔPR-AUC −0.017 [−0.029, −0.006]).

This apparent parity is not stable, and the instability is the finding. The hybrid's standing relative to the physics models is fragile to the single operational rate constant b_op: re-running the entire pipeline at b_op = 1.10, 1.15 and 1.20 swings the y30 hybrid-vs-physics verdict between *inseparable* and *physics-beats-hybrid* (Table 2), because the machine-learning stage carries ln(λ_sim) as a feature and selects its blend weight on a nearly flat validation likelihood (the weight lands anywhere from 0.8 to 1.0). The physics-vs-physics verdicts, by contrast, are identical at every b (Table 2). The in-sample-fit value b_op = 1.20 (the one an evaluation that peeked at the test period would select) is exactly the value at which the hybrid appears to *lose* to the physics; the honest b_op = 1.15 erases that gap. We therefore make no ranking claim between the hybrid and the physics models: the defensible statement is that the ML hybrid adds no robust value over a well-fit ETAS, and its apparent rank turns on a calibration choice to which the physics models are immune.

Table 1. *Primary target M≥3.0/30-day, test set (592 positives), at the honest operational calibration b_op = 1.15. The physics models are inseparable except that first-generation ETAS*

beats the Mizrahi inversion; the hybrid is inseparable from all of them and beats the non-clustering baselines, but this parity is not stable in b_op (Table 2).

Predictor	PR-AUC	ROC-AUC	Brier
sv-ETAS	**0.229**	0.877	0.0173
Cascade (ETAS-sim)	0.228	0.876	0.0173
First-generation ETAS	0.223	**0.880**	0.0164
Hybrid + GNSS (placebo-voided)	0.222	**0.883**	0.0165
Hybrid (cascade × ML)	0.218	0.880	0.0165
Mizrahi ETAS (independent)	0.206	0.878	0.0167
Smoothed seismicity	0.125	0.869	0.0192
Poisson climatology	0.124	0.856	0.0176

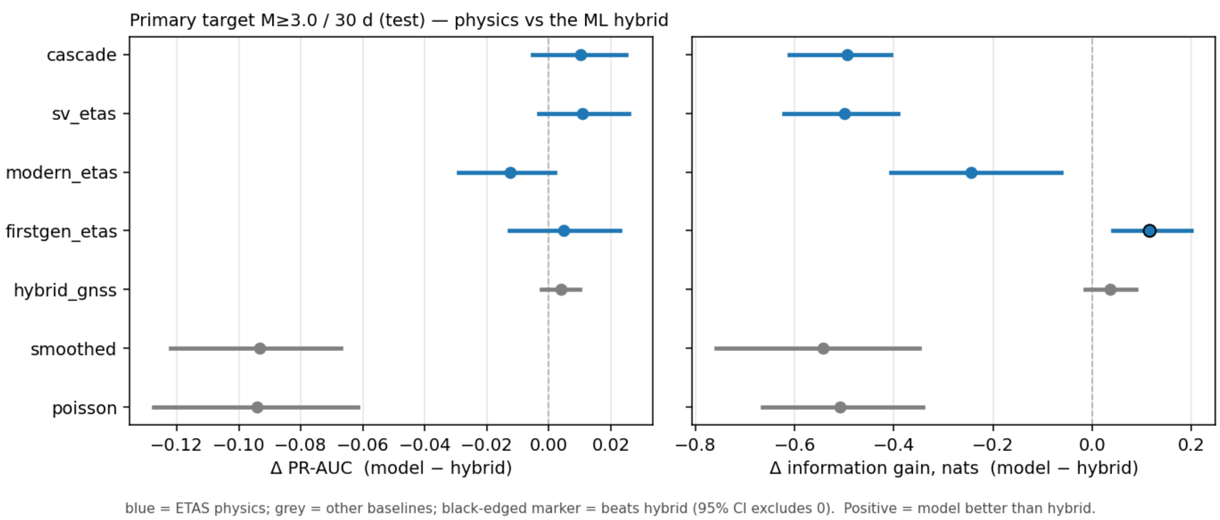

Figure 1: Primary target (M≥3.0/30-day, test set): paired differences (model − hybrid) in PR-AUC (left) and information gain (right) with 95% stationary-block-bootstrap confidence intervals, at the honest b_op = 1.15. Each physics model's interval now straddles zero on at least one axis (inseparable from the hybrid). This parity is not stable: at b_op = 1.20 the physics models beat the hybrid on both axes, and the verdict flips again at b_op = 1.10 (Table 2).

M≥3.5 (Table 3). At M≥3.5 (167 positives) the same instability appears with the opposite sign. At the honest b_op = 1.15 the hybrid (PR-AUC 0.070) now loses to sv-ETAS, Mizrahi and first-generation ETAS on both axes and is inseparable only from the cascade and the non-clustering baselines, whereas at b_op = 1.20 it is inseparable from all of them (Table 2). The physics family is again stable and skilled: cascade ≈ sv-ETAS ≈ first-generation (inseparable), first-generation separably beats Mizrahi, and every ETAS variant beats the Poisson climatology (e.g. cascade +0.79 nats [+0.32, +1.23]); the cascade and sv-ETAS are inseparable from the smoothed baseline on information gain. This replicates, under explicit confidence intervals, the EarthquakeNPP finding that flexible models do not systematically beat ETAS (Stockman et al., 2026): at neither target does the ML variant robustly reach the ETAS family. The value the cascade adds is concentrated *inside active sequences* (where it produces ~1.8× more offspring than first-generation ETAS), the regime where a Marmara sequence would matter.

Table 3. *M≥3.5/30-day, test set (167 positives), b_op = 1.15. The physics models are inseparable among themselves (first-generation beats Mizrahi) and beat Poisson; here the hybrid loses to sv-ETAS/Mizrahi/first-generation, the reverse of the y30 verdict and another symptom of its b-sensitivity (Table 2).*

Predictor	PR-AUC	ROC-AUC	Brier
sv-ETAS	**0.130**	0.880	0.00501
Cascade (ETAS-sim)	0.128	0.882	0.00502
First-generation ETAS	0.126	0.894	**0.00497**
Mizrahi ETAS (independent)	0.110	**0.895**	0.00502
Hybrid (cascade × ML)	0.070	0.884	0.00617
Smoothed seismicity	0.044	0.886	0.00544
Poisson climatology	0.032	0.848	0.00532

Table 2. *Operational-b sensitivity (test split). Re-running the entire pipeline at three operational b (1.15 is the honest pre-2024 optimum) swings the hybrid-vs-physics verdict, while every physics-vs-physics verdict is unchanged. "phys>hyb" = the physics model beats the hybrid on both axes; "insep." = inseparable under the pre-specified rule.*

verdict (test)	b_op = 1.10	b_op = 1.15	b_op = 1.20
y30 hybrid vs cascade	insep.	insep.	phys>hyb
y30 hybrid vs sv-ETAS	insep.	insep.	phys>hyb
y30 hybrid vs Mizrahi	insep.	insep.	phys>hyb
y30 hybrid vs first-gen	phys>hyb	insep.	phys>hyb
y35 hybrid vs cascade	phys>hyb	insep.	insep.
y35 hybrid vs sv-ETAS	insep.	phys>hyb	insep.
y35 hybrid vs Mizrahi	phys>hyb	phys>hyb	insep.

verdict (test)	b_op = 1.10	b_op = 1.15	b_op = 1.20
y35 hybrid vs first-gen	phys>hyb	phys>hyb	insep.
physics vs physics (all pairs, both targets)	*unchanged*	*unchanged*	*unchanged*

M$\geq$4.5 overfit and its fix. On the model box (only 22 test positives) the hybrid overfits: it takes the highest PR-AUC (0.076, above cascade 0.069 and first-generation ETAS 0.067) yet its probabilities are badly miscalibrated, with a *worse* Brier (0.00102 versus the cascade's 0.00068) and a catastrophic information gain against the cascade (-3.763). The strong ranking score on 22 positives is the overfit; the negative IG and worse Brier expose the overconfidence behind it. Training instead on the wide box (593,775 rows, 201 M$\geq$4.5 positives) and evaluating on the model box only drives the selected weight down to w = 0.1 (leaning on the cascade), improves the Brier to 0.00081, and yields IG(hybrid vs cascade) = +1.045 with PR-AUC 0.022 vs 0.008: information gain and PR-AUC now agree. Even here the wide-box IG rests on ~200 positives and shifts under minor catalogue updates, so we treat it as indicative rather than a precise effect size. The production y45 product is the wide-box hybrid; the model-box y45 is diagnostic-only; with only 22 model-box positives the M$\geq$4.5 ranking intervals span zero and support no model ordering, so we make no ranking claim there.

CSEP consistency and the ranking–calibration gap. Over the test period (1,383 observed M$\geq$3.0 events) the catalog-based CSEP tests, computed with pyCSEP (Figure 2), expose a gap between *ranking* skill and *absolute* calibration. At the honest b_op = 1.15 the cascade and sv-ETAS, the top-ranked forecasters, over-predict the count (forecast means 1,498 and 1,489 versus 1,383 observed) and fail the number test, though they remain magnitude-consistent (pyCSEP M-test quantiles 0.062 and 0.055, inside the acceptance band); the independent Mizrahi first-generation inversion under-predicts by 43.4% (782 versus 1,383) and fails both the number and the magnitude tests, because a first-generation intensity without secondary triggering cannot reproduce the aftershock population. No forecaster is number-consistent at the honest calibration, and the cascade's N-test outcome itself depends on b_op (it passes marginally at the leaky b_op = 1.20 and fails at 1.15); this is the same operational fragility as in Table 2. The spatial and pseudo-likelihood tests reject every model, an artifact of the cell-independent Poisson catalogues under-dispersing relative to real clustering, not evidence against the spatial forecast; the pyCSEP and independent in-house N/M verdicts agree for all three models. Strong rank-ordering skill therefore coexists with an unreliable absolute rate that cannot be pinned without an in-sample calibration that would itself leak.

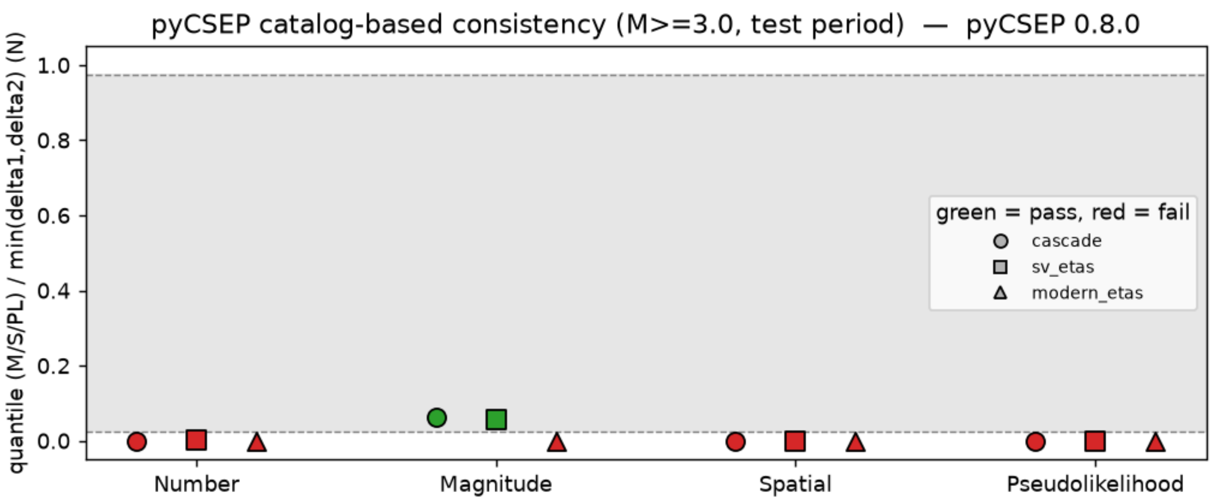

Figure 2: pyCSEP catalog-based consistency tests (M≥3.0, test period) at the honest calibration b_op = 1.15: quantiles of the number, magnitude, spatial and pseudo-likelihood tests (green = consistent at α = 0.05, red = rejected). The top-ranked cascade and sv-ETAS over-predict the count and fail the number test while remaining magnitude-consistent; the independent Mizrahi first-generation inversion under-counts and fails both. The spatial and pseudo-likelihood tests reject all models through Poisson-catalogue under-dispersion.

Engineered non-catalogue channels: a placebo-controlled null. Two engineered channels were tested under the pre-specified gate and the placebo battery, and neither was promoted. The GNSS deformation channel appeared to help: added to the hybrid it raised the channel-level information gain on the M≥3.5 target by +0.098 nats, and on the M≥3.0 target the augmented hybrid beat the plain hybrid on both axes by the bootstrap rule alone. The placebo battery voids both (Figure 3). For the M≥3.5 channel gain, a time-shuffled GNSS series produces a *larger* mean gain (+0.119 nats) and a circularly-shifted one +0.088, straddling the real +0.098, whose own 95% interval [−0.016, +0.207] includes zero. On the M≥3.0 operational target, the real ΔPR-AUC

(+0.033) lies inside the placebo null band [−0.003, +0.063] and the real Δ information gain (+1.18) inside [−0.12, +1.25], with ~60% of the apparent gain from a single window. We report GNSS as a null that supersedes the earlier static-strain null with a stronger, feature-engineering-robust one and offers a concrete demonstration that a confidence interval excluding zero is necessary but not sufficient evidence of a real effect. The dense sub-Mc3 catalogue (an AFAD bulletin homogenized to 10,610 model-box events, 2,276 of them unique events below KOERI completeness, the remainder overlapping KOERI) likewise failed the gate: its test information gain was positive and interval-significant (+0.130 [0.045, 0.229]) but its *validation* gain was negative (−0.030). This validation/test sign disagreement is consistent with completeness non-stationarity, so under the pre-specified promotion rule (validation IG > +0.02 and test IG > 0) it was not adopted. A repeating-earthquake creep channel was designed but its catalogue is not openly available; it is reported as absent, not null.

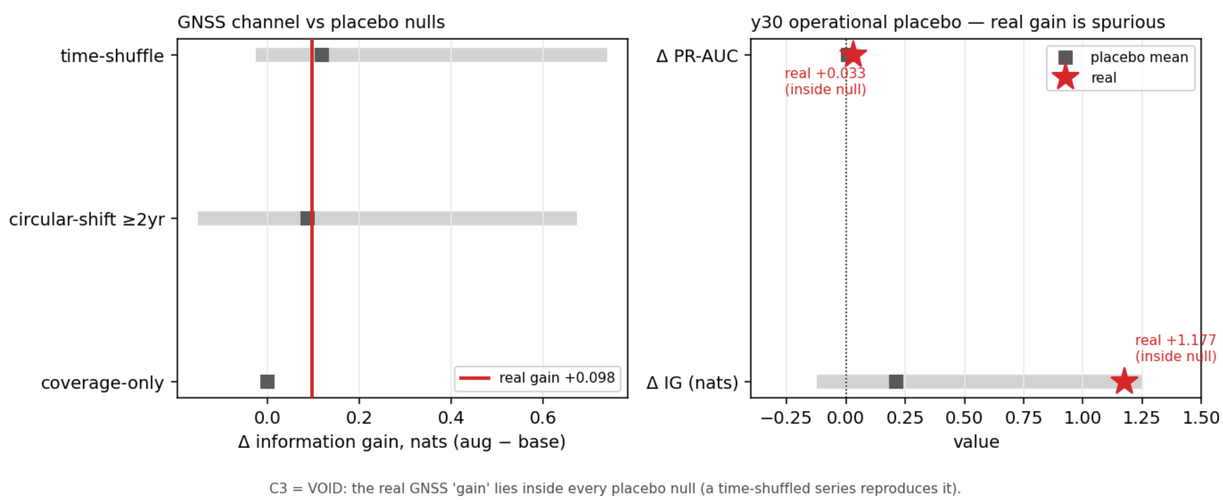

Figure 3: The GNSS channel is a null. Left: the real information gain from adding GNSS (+0.098 nats, red) lies inside the time-shuffle and circular-shift placebo null bands, whose means straddle it. Right: the operational ΔPR-AUC (+0.033) and Δ(information gain) (+1.18) both fall inside their placebo nulls. A randomized GNSS series reproduces the apparent gain.

Calibration (Table S4). A pseudo-prospective calibration battery (2022 → 2026-03) finds every product calibrated in the mean: obs/exp is 1.07 for y35, 1.33 for y45, 0.75 for P(M≥5), 0.84 for P(M≥5.5), and 1.0 for P(M≥6): the last is a single observed event against 1.0 expected, within

Poisson noise. In shape, y35 is calibrated (reliability slope 1.026); the model-box y45 is underfit (slope 1.323, isotonic on the few validation positives being insufficient), which is exactly why the wide-box w = 0.1 variant is the production choice; the M≥5/5.5/6 products are too rare per cell to bin and are reported through the aggregate only. No recalibration erodes skill: at y35 the cascade and hybrid keep positive IG against Poisson, fault-proximity, and smoothed baselines.

Conditional large-event discriminator (Figure 4). With a simulation-disjoint train/test split (so that the 1/3/7-day snapshots of the same simulated trigger never straddle the boundary), the synthetic discriminator is weak: test PR-AUC 0.119 and ROC-AUC 0.622, only about 2.3× the base rate (5.1%). An earlier random row-level split leaked near-duplicate snapshots across the boundary and inflated these to 0.180/0.738; we report the disjoint-split numbers. Applied to the real 2025 sequences with no retraining, it still ranks the escalating sequence above the decaying one (the Sındırgı doublet scores 0.004 versus ~0.0001 for the Kumburgaz sequence), but both scores are low. Consistent with the physics, the same synthetic framework returns a clear null for short-term M≥5.5 predictability from seismicity features (PR-AUC ~0.03, IG ≈ 0 vs sim-Poisson): even with ETAS ground truth, large-event timing is close to a clustering-modulated Poisson process, and the discriminator's limited skill is itself an instance of that null.

Information-arrival analysis of the 2025 events (Figures 5–6). We apply the information-arrival method to three 2025 Marmara events, which between them exercise the method's diagnostic range. The 23 April Mw 6.2 is the primary example (Figure 5). Its spatial part is mature: at a strictly causal freeze the day before, the epicentral cell was the 99.3rd-percentile cell by P(M≥6), a gain of 5.11× over a uniform baseline (Figure 6). Its temporal part shows near-unforecastability: across the freeze schedule (T−365 d, T−180 d, . . . , T−1 h) the epicentral percentile stays flat at ~98–99 all year (persistent fault hazard) while the 30-day M≥6 probability gain stays ~5–8×, and the cell was quiescent throughout (0–2 M≥2 events per 30 d). Only the lone foreshock (ML 4.0, proxy-Mw 4.5), 36 minutes before the mainshock, changed the picture: ten minutes after it (26 minutes before rupture) the cell jumped to the 99.9th percentile and the M≥6 probability gain rose to 45× (30-day P(M≥6) from ~0.010% to ~0.087%), with the discriminator rising to 0.73 (its recent-sequence

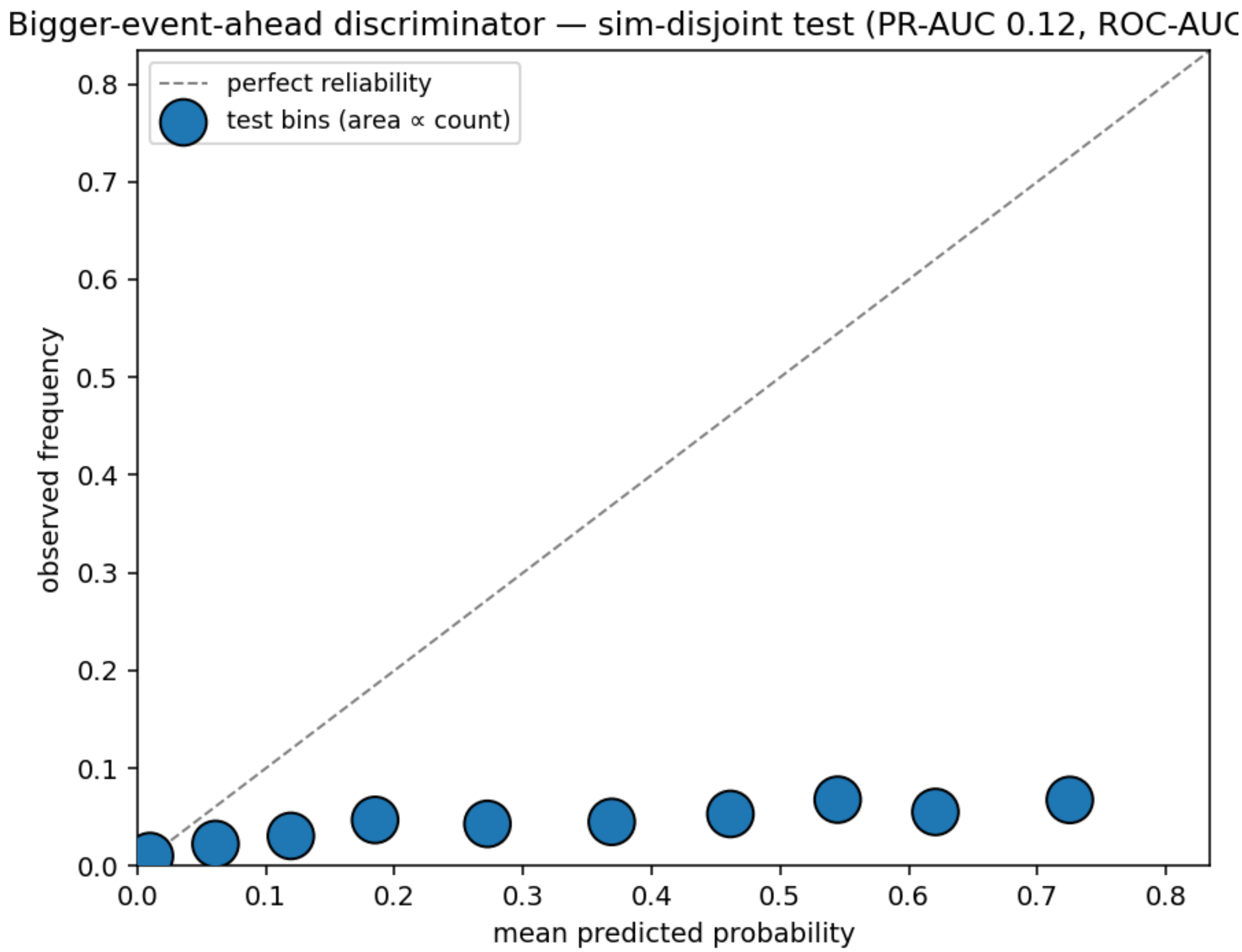

Figure 4: Reliability of the conditional large-event ("bigger-event-ahead") discriminator on simulation-disjoint held-out synthetic sequences (test PR-AUC 0.12, ROC-AUC 0.62). Marker area is proportional to bin count; the dashed line is perfect reliability.

feature mode responds to the developing sequence even though its overall held-out skill is weak). The same feature mode also fired 0.86 at T−90 d on an unrelated cluster away from the eventual epicentre; the discriminator is noisy, and we read it as corroborating rather than primary evidence. The same analysis applied to the neighbouring 2 October 2025 M5.0 shows a different regime: there the discriminator did respond earlier (rising to ~0.65 in the weeks before), consistent with a more sequence-preceded event, though it remains noisy. The 10 August 2025 Sındırgı M6.1 exercises the method's coverage limit: it sits south of the model box and is therefore not spatially covered (percentile 0, a coverage boundary, not a forecasting failure), and its out-of-box discriminator score was a weak ~0.13. Across the three, the method returns the same structural reading (*where* is mature; *when* is bounded by foreshock physics) and quantifies that boundary event by event.

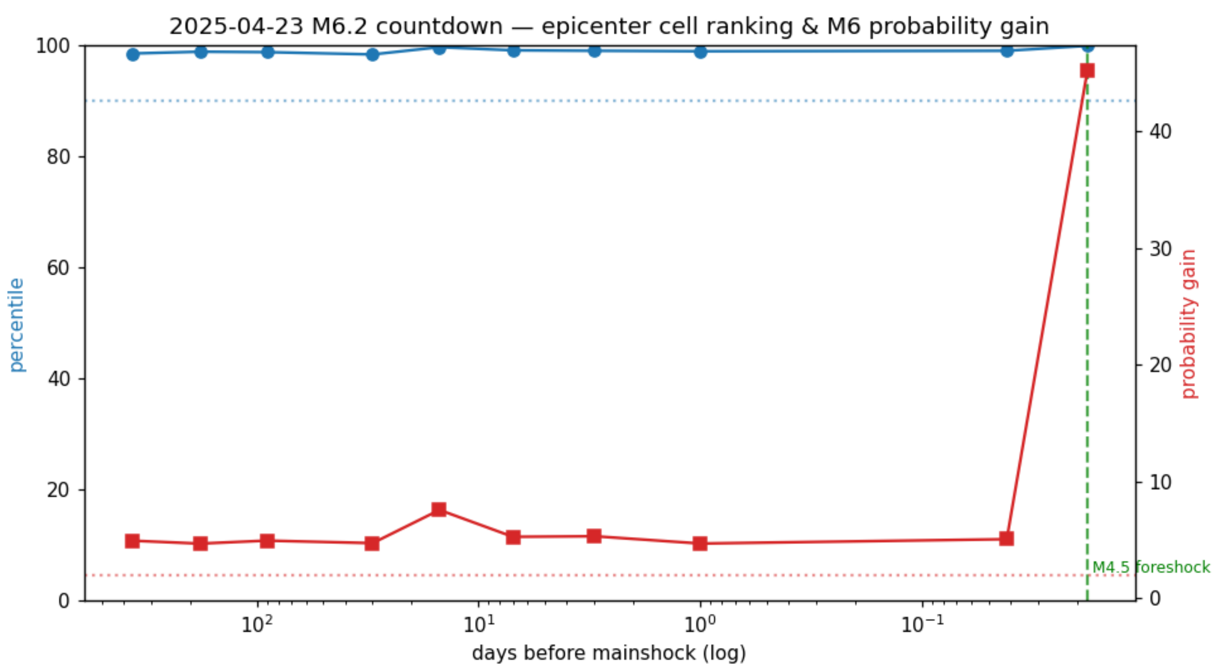

Figure 5: Information-arrival analysis applied to the 23 April 2025 Mw 6.2. Across strictly causal freezes from T−365 d to +10 min, the epicentral-cell percentile stays flat at ~98–99 all year while the 30-day M≥6 probability gain holds at ~5–8×, then jumps to 45× ten minutes after the lone ML 4.0 (proxy-Mw 4.5) foreshock, 26 minutes before the mainshock (the foreshock itself was 36 minutes before). The cell was quiescent throughout.

Live products and horizons. At t0 = 2026-07-05, the live 30-day regional P(M≥6) is 0.13%–4.56% across the b-ensemble, with a central (b_op) value of 1.61% (the spatial M≥3.5

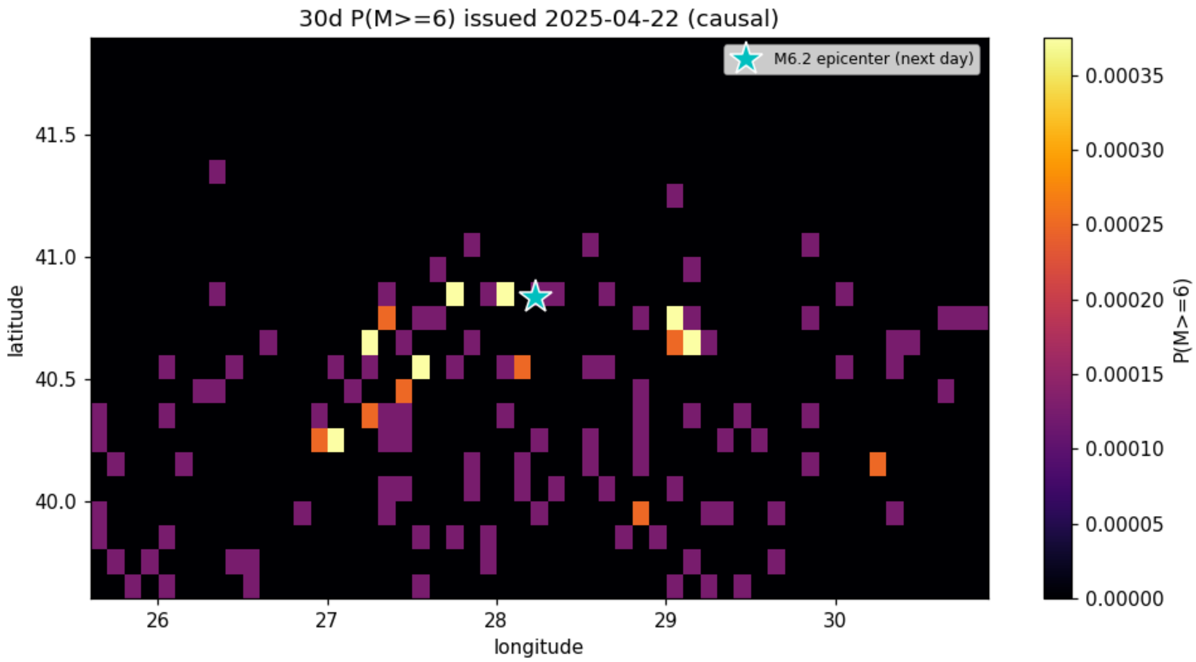

Figure 6: Strictly causal pre-event forecast map for 22 April 2025 (the day before the Mw 6.2). The epicentral cell is the 99.3rd-percentile cell by P(M≥6), a 5.11× gain over a uniform baseline.

product is shown in Figure 7). This central value is of order one percent per month, about the plain-Poisson base rate. The highest 30-day M≥3.5 cell is Armutlu Açıkları–Yalova (28.75° E, 40.55° N, P ≈ 20%), with the 2025 Mw 6.2 aftershock zone at comparable probability. The forecast is issued at every threshold, not only M≥6: the 30-day regional P(M≥5) is 3.7%–38.6% and P(M≥5.5) 0.7%–14.2% across the b-ensemble, with per-cell 30-day maps for the calibrated M≥3.5 and M≥4.5 products (Table S4). Quarter- and year-ahead products are backtest-scaled: pseudo-prospective backtests at four epochs (2022–2025) and two horizons (90 d and 365 d), on regional M≥4.5 counts, give an aggregate reliability slope of 0.97 (within [0.7, 1.3]), so the global scaling factor is 1.0; the central-b_op P(M≥6) is 5.61% over a quarter and 20.6% over a year.

Renewal and extension sources. The Brownian-Passage-Time renewal layer gives 30-year conditional M~7 probabilities of 0.1% for İzmit (ruptured 1999), 8.1% for Ganos, 13.7% for Princes Islands, and 21.8% for Central Marmara/Kumburgaz; the combined Princes + Central 30-year probability of 32.5% is within the Parsons (2004) 30–50% ballpark (sanity anchor passes).

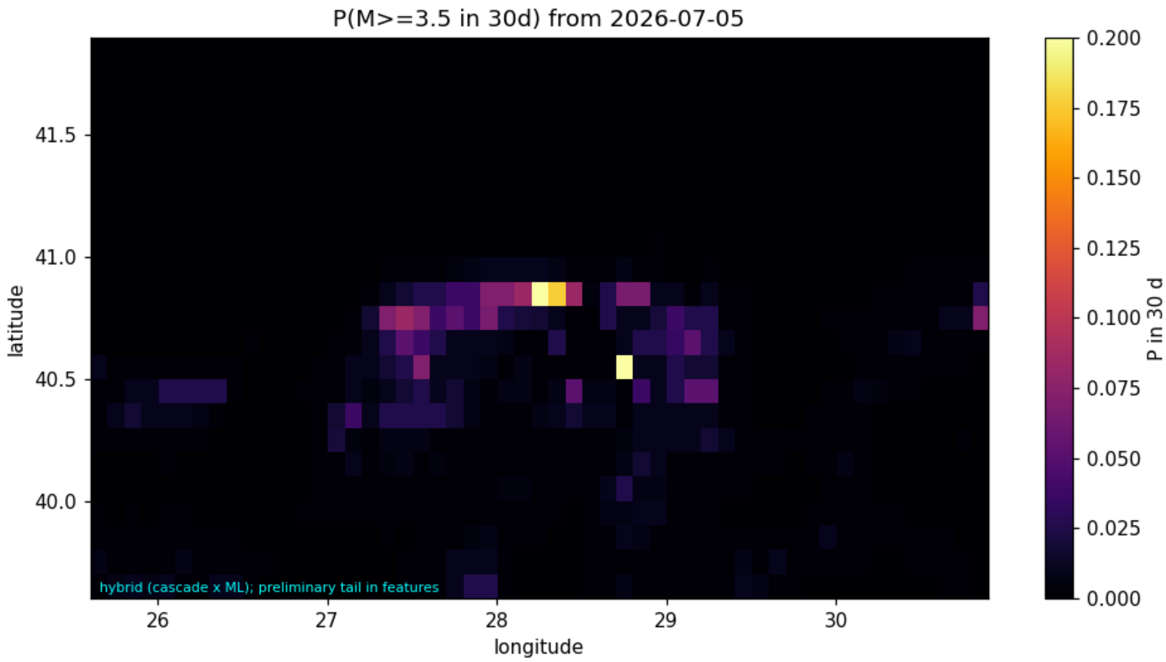

Figure 7: Live 30-day probability of an M≥3.5 event per 0.1° cell at t0 = 2026-07-05. Probability concentrates along the Main Marmara Fault, on the 2025 Mw 6.2 aftershock zone and an Armutlu–Yalova cluster; the highest cell is P ≈ 20%.

5. Discussion

A central result of this study is a where-vs-when decomposition. The spatial forecasting problem for Marmara is, in an operational sense, mature: the seismicity-feature model concentrates probability on the correct fault cells, and in the Mw 6.2 case the epicentral cell was persistently in the top ~1% of cells for a full year before the event, a 5.11× probability gain over a uniform baseline at the day-before freeze. The temporal problem is different in kind. The information-arrival analysis shows that the specific *timing* of the Mw 6.2 was near-unforecastable from the catalogue: the cell was quiescent, and the only short-term information arrived with the lone ML 4.0 (proxy-Mw 4.5) foreshock, 36 minutes before the mainshock. The method quantifies this boundary: the gain is flat at 5–8× for a year, then jumps to 45× ten minutes after the foreshock. Run across the three 2025 events, it locates each on the same where-mature / when-foreshock-bounded axis.

This decomposition reconciles our results with the broader literature. The EarthquakeNPP benchmark found that flexible models do not beat ETAS (Stockman et al., 2026); our benchmark reaches the same conclusion by a sharper route. The physics forecasters (first-generation, cascade, spatially-variable-background, and an independent inversion) are mutually inseparable and *stable*: their pairwise verdicts do not move when the operational rate constant is varied. The ETAS$\times$ML hybrid has no such stability. Because its machine-learning stage takes the cascade rate as a feature and selects its blend weight on a nearly flat validation likelihood, a change of about 0.05 in the operational b flips its verdict against the physics models, from inseparable to losing, at both targets and with no consistent direction (Table 2). The honest reading is therefore that **the ML hybrid adds no robust value over a well-fit ETAS**: where it appears to win or lose is an artifact of a calibration choice to which the physics models are immune. We do not claim that physics beats the machine learning, nor that the two are equivalent. This is a stronger form of the EarthquakeNPP message: once leakage is removed, the seismicity-only signal is close to what ETAS already extracts, and the added flexibility buys mostly fragility. Where our cascade does add value (inside active sequences, and in the analytic per-cell rare-rate field that supports the countdown), it does so through better physics, not a more flexible regressor.

A second methodological theme is that statistical significance is not enough without placebo controls. Two engineered channels, GNSS deformation and a dense sub-Mc3 catalogue, each produced an information gain whose block-bootstrap interval excluded zero, the conventional bar for a positive result; yet a time-shuffled or circularly-shifted surrogate of the GNSS channel reproduced the same gain, and the dense channel reversed sign between validation and test. Both are nulls. The general lesson for spatiotemporal seismicity machine learning is that information-gain or confidence-interval evidence is insufficient on its own: a candidate feature channel should be required to beat label-shuffled and time-shifted versions of itself, because block-bootstrap significance can certify structured noise. In our own workflow the GNSS channel initially cleared the interval-significance bar and was flagged for promotion; the placebo battery then voided it. That promote-then-void sequence is precisely why we adopted the battery as a standing requirement rather than an afterthought.

A further theme is conditional forecastability. The synthetic discriminator ranks sequence-preceded escalation (Sındırgı) far above cold-start decay (Kumburgaz), suggesting that the regime in which short-term large-event forecasting has traction is the sequence-preceded one. This is the same regime the Foreshock Traffic-Light System targets (Gulia & Wiemer, 2019; Gulia et al., 2020), though our FTLS overlay never classified the cold-start Kumburgaz sequence (it stayed below the event count the system requires) and reached red only for the more developed Sındırgı sequence. The operational implication for Marmara is a sequence mode: a persistent spatial hazard map, augmented by sequence-triggered alerts when foreshock-like b-value drops appear, with the explicit understanding that cold-start mainshocks (of which the Mw 6.2 was effectively one) will not be caught in time. This conclusion carries an explicit ceiling: the discriminator is trained on ETAS simulations, so by construction it can only detect the escalation statistics ETAS itself generates and cannot see beyond-ETAS precursory physics; the Sındırgı-versus-Kumburgaz separation is an illustrative contrast on two real sequences ($n = 2$), not a calibrated skill estimate. This ceiling is specific to the synthetic layer, and the distinction matters for the study as a whole: the benchmark's machine-learning stage is trained on real catalogue features against real outcomes and was offered non-ETAS channels (Coulomb stress, geodetic deformation, sub-completeness seismicity, local b-value structure), so it could in principle have discovered information absent from ETAS. The finding is that, under placebo control, it did not. Every component of the study answers that single question: the ETAS variants as fair baselines, the placebo battery as the channel control, the synthetic and renewal layers as the only honest route to M6 statements, the prospective log as the forward commitment.

Third, our audit-first design speaks directly to the reliability of multi-source "accuracy" claims in the machine-learning seismicity literature. Studies that evaluate on random splits, or add exotic data sources without a causality gate, routinely report skill that does not survive forward validation; our benchmark makes the opposite bet: a smaller, sometimes negative, but *machine-checkably causal* set of numbers.

A further point: the audit changes which results are believable, not only their size. The sparse model-box y45 target illustrates this: the highest PR-AUC (0.076) coexists with a *worse*

Brier score and a catastrophic information gain against the cascade (-3.763), a combination that is only interpretable as overfitting to 22 positives. A pipeline that trusted the ranking score alone, without a calibration battery and without the discipline of requiring IG and PR-AUC to agree, would have reported the top PR-AUC as skill. The wide-box remedy regularises the weight to w = 0.1 and brings the two metrics into agreement. We report such disagreements and null results, like the STAI correction and the GNSS feature, as part of the benchmark.

Finally, on responsible communication: we report probability *gain* relative to base rates. The live regional 30-day M$\geq$6 probability is of order one percent, consistent with the long-term rate; the renewal layer's decade- scale probabilities for the locked central segment are elevated but consistent with prior hazard estimates (Parsons, 2004). Nothing in these results implies an imminent large earthquake, and the eastward-migration context (Martínez-Garzón et al., 2026) should be communicated as a long-term hazard, not a short-term forecast. The appropriate operational posture is therefore a standing, well-calibrated spatial hazard map that is transparent about its temporal limits, plus a sequence-triggered alert layer whose false-alarm and miss characteristics are stated up front.

6. Limitations and future work

Several limitations bound the results. The study covers a single region with a single real M6, so the large-event results rest on synthetic validation and wide-box percentile checks rather than direct classification, and the M$\geq$4.5 target is unpowered (22 model-box positives), supporting no ranking claim. The negative machine-learning result is therefore best read as a single-region confirmation, under stricter leakage control, of the multi-region EarthquakeNPP finding (Stockman et al., 2026); the audit machinery is region-agnostic, and the open, machine-checkable gates are a direct invitation to replicate it elsewhere. The test set was scored more than once over the study; every such evaluation was an identical-configuration deterministic reproduction and all hyperparameters, including the hybrid weight w, were selected on the validation split alone, so no test-set information entered model selection, but we disclose the repeated scoring rather than claim a single-touch ideal. The live forecast uses a *preliminary* catalogue tail (features only; excluded from every metric), whose magnitudes are untyped. The b-value uncertainty dominates all M6 extrapolation: the mixed Md/ML catalogue inflates b-positive to ~1.54, and the M6 rate can differ several-fold across the ensemble, so we report the ensemble range, not a point estimate. The completeness structure is a genuine mixture (Md and ML populations complete at different magnitudes), handled with a consistent conservative Mc but limiting how low the target magnitude can go. The ETAS fit is isotropic and pinned at the 0.95 branching cap (the STAI and un-pinning attempts returned nulls), and the backtest cascade is limited to K = 500 sims, which bounds the resolution of the rarest per-cell rates. The CSEP spatial and pseudo-likelihood tests are confounded by the cell-independent Poisson catalogues and are not interpretable here; a native-clustered-catalogue S-test is the correct refinement. The GNSS null is specific to this network and feature representation: the continuous-GPS geometry is weak against the offshore Main Marmara Fault, whose deformation is poorly resolved by onshore stations, so it bounds this channel as engineered, not geodetic coupling in general. The Sındırgı sequence exposed a hard spatial-coverage limit of the model box.

Future work follows from the results. A dense, machine-learning-repicked micro-catalogue (Mc ~ 1.5) remains the highest-value data lever, but our first attempt at one, an AFAD sub-Mc3 bulletin, failed the pre-specified promotion gate through a validation/test sign disagreement consistent with completeness non-stationarity, so the lever is a per-year-completeness-normalised feature set on a longer validation window rather than raw dense counts. Time-variable GNSS coupling on an offshore-sensitive geometry and repeating-earthquake creep observables are the next two physical levers, both currently limited by data availability (the repeater catalogue was designed for but is not openly available). Finally, the prospective, hashed forecast log should be allowed to accumulate: only an out-of-sample record, which a backtest cannot substitute for, can establish whether the mature spatial skill demonstrated here translates into operational value.

Supplementary material

The supplementary file contains Table S1 (principal Coulomb stress sources), Table S2 (the 19 causal features), Table S3 (catalogue summary), Table S4 (the calibration battery), and Figure S1 (the first-generation versus EM-declustered background rate fields).

Data and code availability

All code, processed data products, configuration files, and results artifacts associated with this study are archived on Zenodo at https://doi.org/10.5281/zenodo.21224503 (Alhan & Khabat, 2026) and developed at https://github.com/keremalhan/marmara-forecast. The archive includes the block-bootstrap confidence intervals and the machine-readable claims file that adjudicates every model comparison, the GNSS and dense-catalogue placebo-battery outputs, the pyCSEP catalog inputs and consistency-test results, and the AFAD dense-catalogue build report; the append-only, hash-stamped prospective forecast log continues to accumulate beyond the archived snapshot.

The processed catalogue is redistributed as a derived dataset with attribution to the Boğaziçi University Kandilli Observatory and Earthquake Research Institute Regional Earthquake-Tsunami Monitoring Center (KOERI-RETMC). GNSS velocity inputs are from the Nevada Geodetic Laboratory, and fault geometry inputs are from the GEM Global Active Faults Database. Full data-use and software license information is provided in the archived repository.

Author contributions

Basri Kerem Alhan: Conceptualization, Methodology, Data curation, Writing – original draft.
Kenessary Khabat: Software, Formal analysis, Writing – review & editing.

Competing interests

The authors declare no competing interests.

Acknowledgements

We thank the Boğaziçi University Kandilli Observatory and Earthquake Research Institute Regional Earthquake-Tsunami Monitoring Center (KOERI-RETMC) for the earthquake bulletin that underlies the catalogue, the Nevada Geodetic Laboratory for the GNSS velocity solutions, and the GEM Global Active Faults Database for the fault model. This research received no external funding.

References

Aki, K. (1965). Maximum likelihood estimate of b in the formula $\log N = a - bM$ and its confidence limits. *Bulletin of the Earthquake Research Institute, 43*, 237–239.

Alhan, B. K., & Khabat, K. (2026). *Code and data for: Leakage-audited machine learning versus ETAS for earthquake forecasting in the Sea of Marmara* (Version 1.1.0) [Software]. Zenodo. https://doi.org/10.5281/zenodo.21224503

Ambraseys, N. (2002). The seismic activity of the Marmara Sea region over the last 2000 years. *Bulletin of the Seismological Society of America, 92*(1), 1–18. https://doi.org/10.1785/0120000843

Barka, A., Akyüz, H. S., Altunel, E., Sunal, G., Çakir, Z., Dikbas, A., Yerli, B., Armijo, R., Meyer, B., de Chabalier, J. B., Rockwell, T., Dolan, J. R., Hartleb, R., Dawson, T., Christofferson, S., Tucker, A., Fumal, T., Langridge, R., Stenner, H., … Page, W. (2002). The surface rupture and slip distribution of the 17 August 1999 İzmit earthquake (M 7.4), North Anatolian Fault. *Bulletin of the Seismological Society of America, 92*(1), 43–60. https://doi.org/10.1785/0120000841

Blewitt, G., Hammond, W. C., & Kreemer, C. (2018). Harnessing the GPS data explosion for interdisciplinary science. *Eos, 99*. https://doi.org/10.1029/2018EO104623

Dascher-Cousineau, K., Shchur, O., Brodsky, E. E., & Günnemann, S. (2023). Using deep learning for flexible and scalable earthquake forecasting. *Geophysical Research Letters, 50*(17), e2023GL103909. https://doi.org/10.1029/2023GL103909

Ertuncay, D., Büyükakpınar, P., Fornasari, S. F., & Tan, O. (2025). 23 April 2025 Marmara Sea (Mw 6.3), Türkiye earthquake: Mainshock, aftershock, and ground observations. *Seismica,* *4*(2), 1773. https://doi.org/10.26443/seismica.v4i2.1773

Gulia, L., & Wiemer, S. (2019). Real-time discrimination of earthquake foreshocks and aftershocks. *Nature, 574*(7777), 193–199. https://doi.org/10.1038/s41586-019-1606-4

Gulia, L., Wiemer, S., & Vannucci, G. (2020). Pseudoprospective evaluation of the foreshock traffic-light system in Ridgecrest and implications for aftershock hazard assessment. *Seismological Research Letters, 91*(5), 2828–2842. https://doi.org/10.1785/0220190307

Hainzl, S., Kumazawa, T., & Ogata, Y. (2024). Aftershock forecasts based on incomplete earthquake catalogues: ETASI model application to the 2023 SE Türkiye earthquake sequence. *Geophysical Journal International, 236*(3), 1609–1620. https://doi.org/10.1093/gji/ggae006

Hardebeck, J. L., Llenos, A. L., Michael, A. J., Page, M. T., Schneider, M., & van der Elst, N. J. (2024). Aftershock forecasting. *Annual Review of Earth and Planetary Sciences, 52*, 61–84. https://doi.org/10.1146/annurev-earth-040522-102129

Helmstetter, A., Kagan, Y. Y., & Jackson, D. D. (2006). Comparison of short-term and time-independent earthquake forecast models for southern California. *Bulletin of the Seismological Society of America, 96*(1), 90–106. https://doi.org/10.1785/0120050067

Jover-Alfaro, J., Arias-Antúnez, E., & Mateo-Cortés, J. (2026). Forecasting earthquakes by Machine Learning techniques: lights and shadows. *Earth Science Informatics, 19*, 24. https://doi.org/10.1007/s12145-026-02078-x

Kadirioğlu, F. T., & Kartal, R. F. (2016). The new empirical magnitude conversion relations using an improved earthquake catalogue for Turkey and its near vicinity (1900–2012). *Turkish Journal of Earth Sciences, 25*(4), 300–310. https://doi.org/10.3906/yer-1511-7

Karabulut, H., Güvercin, S. E., Eskiköy, F., Konca, A. Ö., & Ergintav, S. (2021). The moderate size 2019 September Mw 5.8 Silivri earthquake unveils the complexity of the Main Marmara Fault shear zone. *Geophysical Journal International, 224*(1), 377–388. https://doi.org/10.1093/gji/ggaa469

King, G. C. P., Stein, R. S., & Lin, J. (1994). Static stress changes and the triggering of earthquakes. *Bulletin of the Seismological Society of America, 84*(3), 935–953.

https://doi.org/10.1785/BSSA0840030935

Martínez-Garzón, P., Chen, X., Becker, D., Núñez-Jara, S., Kartal, R. F., Türker, E., Dresen, G., Ben-Zion, Y., Jara, J., Cotton, F., Kadirioğlu, F. T., Kılıç, T., & Bohnhoff, M. (2026). Progressive eastward rupture of the Main Marmara Fault toward Istanbul. *Science, 391*(6783), 379–383. https://doi.org/10.1126/science.adz0072

Matthews, M. V., Ellsworth, W. L., & Reasenberg, P. A. (2002). A Brownian model for recurrent earthquakes. *Bulletin of the Seismological Society of America, 92*(6), 2233–2250. https://doi.org/10.1785/0120010267

Mizrahi, L., Nandan, S., & Wiemer, S. (2021). The effect of declustering on the size distribution of mainshocks. *Seismological Research Letters, 92*(4), 2333–2342. https://doi.org/10.1785/0220200231

Mizrahi, L., Dallo, I., van der Elst, N. J., Christophersen, A., Spassiani, I., Werner, M. J., Iturrieta, P., Bayona, J. A., Iervolino, I., Schneider, M., Page, M. T., Zhuang, J., Herrmann, M., Michael, A. J., Falcone, G., Marzocchi, W., Rhoades, D., Gerstenberger, M., Gulia, L., Schorlemmer, D., Becker, J., Han, M., Kuratle, L., Marti, M., & Wiemer, S. (2024). Developing, testing, and communicating earthquake forecasts: Current practices and future directions. *Reviews of Geophysics, 62*(3), e2023RG000823. https://doi.org/10.1029/2023RG000823

Ogata, Y. (1988). Statistical models for earthquake occurrences and residual analysis for point processes. *Journal of the American Statistical Association, 83*(401), 9–27. https://doi.org/10.1080/01621459.1988.10478560

Okada, Y. (1992). Internal deformation due to shear and tensile faults in a half-space. *Bulletin of the Seismological Society of America, 82*(2), 1018–1040. https://doi.org/10.1785/BSSA0820021018

Parsons, T. (2004). Recalculated probability of M $\geq$ 7 earthquakes beneath the Sea of Marmara, Turkey. *Journal of Geophysical Research: Solid Earth, 109*(B5), B05304. https://doi.org/10.1029/2003JB002667

Politis, D. N., & Romano, J. P. (1994). The stationary bootstrap. *Journal of the American Statistical Association, 89*(428), 1303–1313. https://doi.org/10.1080/01621459.1994.10476870

Rhoades, D. A., Schorlemmer, D., Gerstenberger, M. C., Christophersen, A., Zechar, J. D., & Imoto, M. (2011). Efficient testing of earthquake forecasting models. *Acta Geophysica, 59*(4), 728–747. https://doi.org/10.2478/s11600-011-0013-5

Savran, W. H., Werner, M. J., Marzocchi, W., Rhoades, D. A., Jackson, D. D., Milner, K., Field, E., & Michael, A. (2020). Pseudoprospective evaluation of UCERF3-ETAS forecasts during the 2019 Ridgecrest sequence. *Bulletin of the Seismological Society of America, 110*(4), 1799–1817. https://doi.org/10.1785/0120200026

Savran, W. H., Bayona, J. A., Iturrieta, P., Asim, K. M., Bao, H., Bayliss, K., Herrmann, M., Schorlemmer, D., Maechling, P. J., & Werner, M. J. (2022). pyCSEP: A Python toolkit for earthquake forecast developers. *Seismological Research Letters, 93*(5), 2858–2870. https://doi.org/10.1785/0220220033

Stockman, S., Lawson, D. J., & Werner, M. J. (2026). EarthquakeNPP: A benchmark for earthquake forecasting with neural point processes. *Transactions on Machine Learning Research.* https://openreview.net/forum?id=dIcNAg6ZuZ

Styron, R., & Pagani, M. (2020). The GEM Global Active Faults Database. *Earthquake Spectra, 36*(S1), 160–180. https://doi.org/10.1177/8755293020944182

van der Elst, N. J. (2021). B-positive: A robust estimator of aftershock magnitude distribution in transiently incomplete catalogs. *Journal of Geophysical Research: Solid Earth, 126*(2), e2020JB021027. https://doi.org/10.1029/2020JB021027

Veen, A., & Schoenberg, F. P. (2008). Estimation of space–time branching process models in seismology using an EM-type algorithm. *Journal of the American Statistical Association, 103*(482), 614–624. https://doi.org/10.1198/016214508000000148

Wiemer, S., & Wyss, M. (2000). Minimum magnitude of completeness in earthquake catalogs: Examples from Alaska, the western United States, and Japan. *Bulletin of the Seismological Society of America, 90*(4), 859–869. https://doi.org/10.1785/0119990114

Yavas, C. E., Chen, L., Kadlec, C., & Ji, Y. (2024). Improving earthquake prediction accuracy in Los Angeles with machine learning. *Scientific Reports, 14*, 24440. https://doi.org/10.1038/s41598-

024-76483-x (Retraction published 2026, https://doi.org/10.1038/s41598-026-49689-4)

Zechar, J. D., & Jordan, T. H. (2008). Testing alarm-based earthquake predictions. *Geophysical Journal International, 172*(2), 715–724. https://doi.org/10.1111/j.1365-246X.2007.03676.x

Zhuang, J., Ogata, Y., & Vere-Jones, D. (2002). Stochastic declustering of space–time earthquake occurrences. *Journal of the American Statistical Association, 97*(458), 369–380. https://doi.org/10.1198/016214502760046925